ACS NANO

www.acsnano.org

ARTICLE

Surface-Charge-Switchable Nanoclusters for Magnetic Resonance Imaging-Guided and Glutathione Depletion-Enhanced Photodynamic Therapy

Jianzhi Zhu,[#] Tingting Xiao,[#] Jiulong Zhang, Hailong Che, Yuxin Shi, Xiangyang Shi,* and Jan C. M. van Hest*

Cite This: *ACS Nano* 2020, 14, 11225–11237

Read Online

ACCESS | Metrics & More | Article Recommendations | Supporting Information

ABSTRACT: Photodynamic therapy (PDT) is an effective noninvasive therapeutic method that employs photosensitizers (PSs) converting oxygen to highly cytotoxic singlet oxygen ($^1O_2$) under light irradiation. The conventional PDT efficacy is, however, compromised by the nonspecific delivery of PSs to tumor tissue, the hypoxic tumor microenvironment, and the reduction of generated $^1O_2$ by the intracellular antioxidant glutathione (GSH). Herein, an intelligent multifunctional synergistic nanoplatform (CMGCC) for T_1-weighted magnetic resonance (MR) imaging-guided enhanced PDT is presented, which consists of nanoparticles composed of catalase (CAT) and manganese dioxide (MnO_2) that are integrated within chlorin-e6-modified glycol chitosan (GC) polymeric micelles. In this system, (1) GC polymers with pH-sensitive surface charge switchability from neutral to positive could improve the PS accumulation within the tumor region, (2) CAT could effectively reoxygenate the hypoxic tumor *via* catalyzing endogenous hydrogen peroxide to O_2, and (3) MnO_2 could consume the intracellular GSH while simultaneously producing Mn^{2+} as a contrast agent for T_1-weighted MR imaging. The CMGCC particles possess uniform size distribution, well-defined structure, favorable enzyme activity, and superior $^1O_2$ generation ability. Both *in vitro* and *in vivo* experiments demonstrate that the CMGCC exhibit significantly enhanced PDT efficacy toward HeLa cells and subcutaneous HeLa tumors. Our study thereby demonstrates this to be a promising synergistic theranostic nanoplatform with highly efficient PDT performance for cancer therapy.

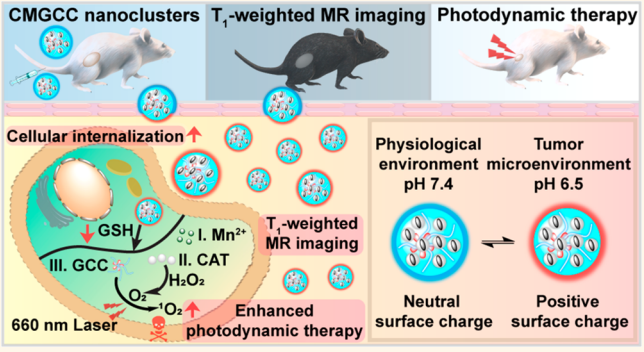

KEYWORDS: *photodynamic therapy, glycol chitosan, manganese dioxide, catalase, magnetic resonance imaging*

Photodynamic therapy (PDT) has emerged as an alternative tumor destruction method to conventional systemic cancer therapy owing to its temporal and spatial control which affords local treatment.[1,2] It requires three intrinsically nontoxic elements: light, oxygen (O_2), and a photosensitizer (PS). Upon light irradiation, a PS can convert O_2 to singlet oxygen ($^1O_2$) immediately and provokes $^1O_2$-induced irreversible oxidation of the adjacent (<0.2 μm) biomacromolecules including DNA, proteins, and membrane lipids, thus leading to the dysfunctioning of intrinsic physiological metabolism.[3] Substantial research has been performed to demonstrate the promising application of PDT as a stand-alone treatment or combined therapeutic modality in early stage antitumor therapy.[4−9] Nevertheless, the therapeutic efficacy of PDT is seriously compromised by (1) nonspecific PS accumulation, (2) the proliferation-induced hypoxic tumor microenvironment, and (3) the diminishing effect of the generated $^1O_2$ by the antioxidant glutathione (GSH), which is overexpressed in cancer cells.[10,11] Therefore, constructing multifunctional nanosystems that can simulta-

Received: April 11, 2020
Accepted: August 11, 2020
Published: August 18, 2020

https://dx.doi.org/10.1021/acsnano.0c03080
ACS Nano 2020, 14, 11225–11237

Scheme 1. Schematic Illustration of Theranostic Functions of the Developed Multifunctional CMGCC Nanocluster, Composed of Catalase-Stabilized MnO_2 Nanoparticles Incorporated into Ce6-Conjugated Glycol Chitosan Micelles[a]

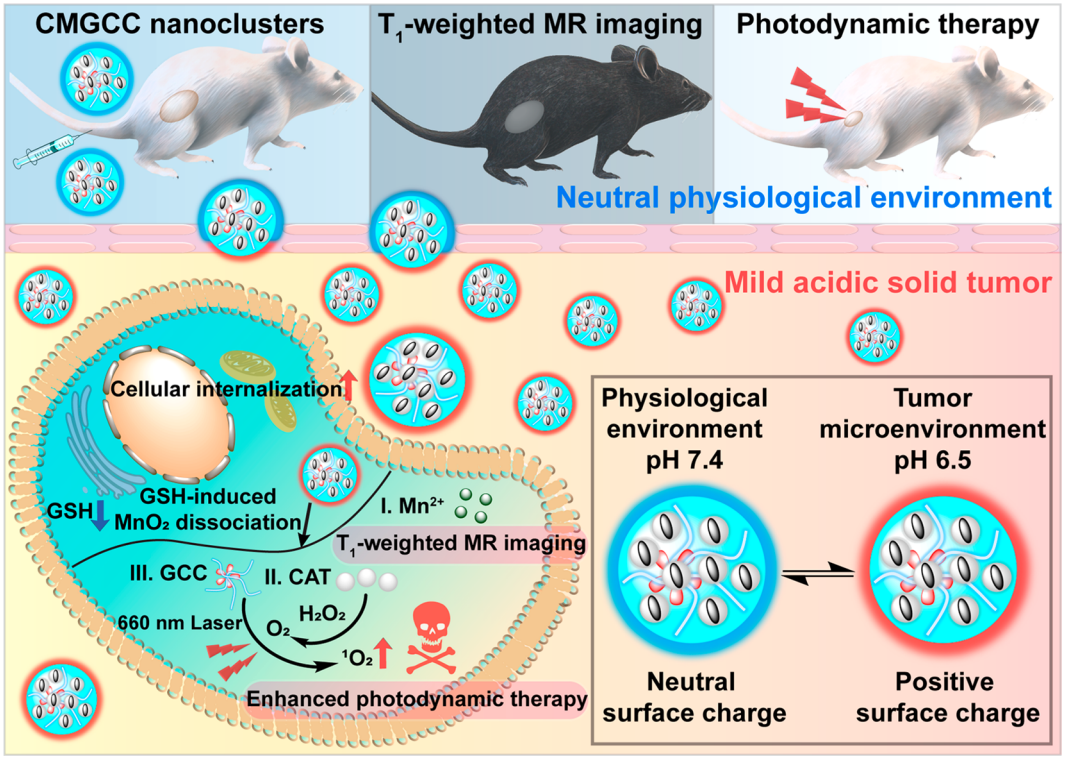

[a]The synergistic therapy process includes the following: (1) GC polymer imparts the system with a neutral surface charge at physiological conditions for prolonged circulation time and a positive surface charge switch within the tumor microenvironment for improved tumor accumulation; (2) CAT can catalyze the conversion of endogenous H_2O_2 to generate O_2 to alleviate tumor hypoxia for production of highly toxic $^1O_2$; (3) MnO_2 can react with intracellular glutathione (GSH) to decrease the GSH-induced $^1O_2$ reduction and simultaneously produce Mn^{2+} ions for T_1-weighted MR imaging.

neously overcome these obstacles is of great importance but also remains a tremendous challenge.

Localized transport of a PS to the targeted cancer tissues, especially to the preferential subcellular organelles, is promising as it elevates tumor-specific $^1O_2$-induced oxidation and subsequent cell death.[12−20] Taking advantage of the slightly acidic tumor microenvironment has become a popular strategy to achieve tumor-targeted PS delivery. Nanoplatforms with a surface charge pH responsiveness have attracted much attention as a neutral or slightly negative surface potential could contribute to prolonged *in vivo* circulation time and reduced nonspecific clearance, whereas a positive charge transition at the tumor region could enhance the tumor retention time and cellular internalization.[21] Although this charge switchability concept is potentially useful, it is often compromised by the lack of biocompatibility and biodegradability of the applied platform components, which limits biomedical applications.[22] Recently, glycol chitosan (GC) polymers have been reported as a favorable biocompatible and biodegradable candidate to fabricate pH-responsive nanoplatforms.[23−27] At a physiological pH 7.4, GC displays a neutral surface charge, affording the platforms low protein absorption and reduced cellular interaction to prolong the *in vivo* blood circulation time. When exposed to the acidic tumor microenvironment pH 6.5, GC exhibits a positive surface charge owing to the protonation of the amine groups, which could thereafter significantly improve the cellular uptake. Therefore, GC-based nanoplatforms are highly promising for enhanced transportation of PS to the tumor region.

The hypoxic tumor microenvironment, which is caused by the increased O_2 consumption of dysregulated tumor cells, considerably restricts PDT efficacy, as PDT is an O_2-dependent modality. Relieving the hypoxic tumor microenvironment is an important key to boost the yield of cytotoxic $^1O_2$.[11,28−36] Considering the high concentrations of endogenous H_2O_2 within the solid tumor, using catalase (CAT) to trigger the catalytic decomposition of H_2O_2 into H_2O and O_2 is a promising strategy to afford reoxygenation, thus enhancing the PDT efficacy.[29,30] It is also known that cancer cells produce a high level of GSH as an antioxidant to protect themselves from the external oxidative stress, including $^1O_2$.[37,38] Depleting the intracellular GSH is thus highly desirable to sensitize tumor cells to PDT.[10,39−41] Manganese dioxide (MnO_2) can exert a redox reaction with GSH to yield glutathione disulfide and Mn^{2+}, thus effectively down-regulating the GSH level, and interestingly, the consequently generated Mn^{2+} can be further used as T_1-weighted magnetic resonance (MR) imaging contrast agents for tumor imaging and detection.[10,42−47] Therefore, the integration of CAT and MnO_2 in the PDT process holds great potential to promote PDT performance by simultaneously reoxygenating the hypoxic tumor tissue, depleting the intracellular GSH, and providing MR imaging guidance.

Herein, we have constructed a multifunctional synergistic nanoplatform for T_1-weighted MR imaging-guided tumor

https://dx.doi.org/10.1021/acsnano.0c03080
ACS Nano 2020, 14, 11225−11237

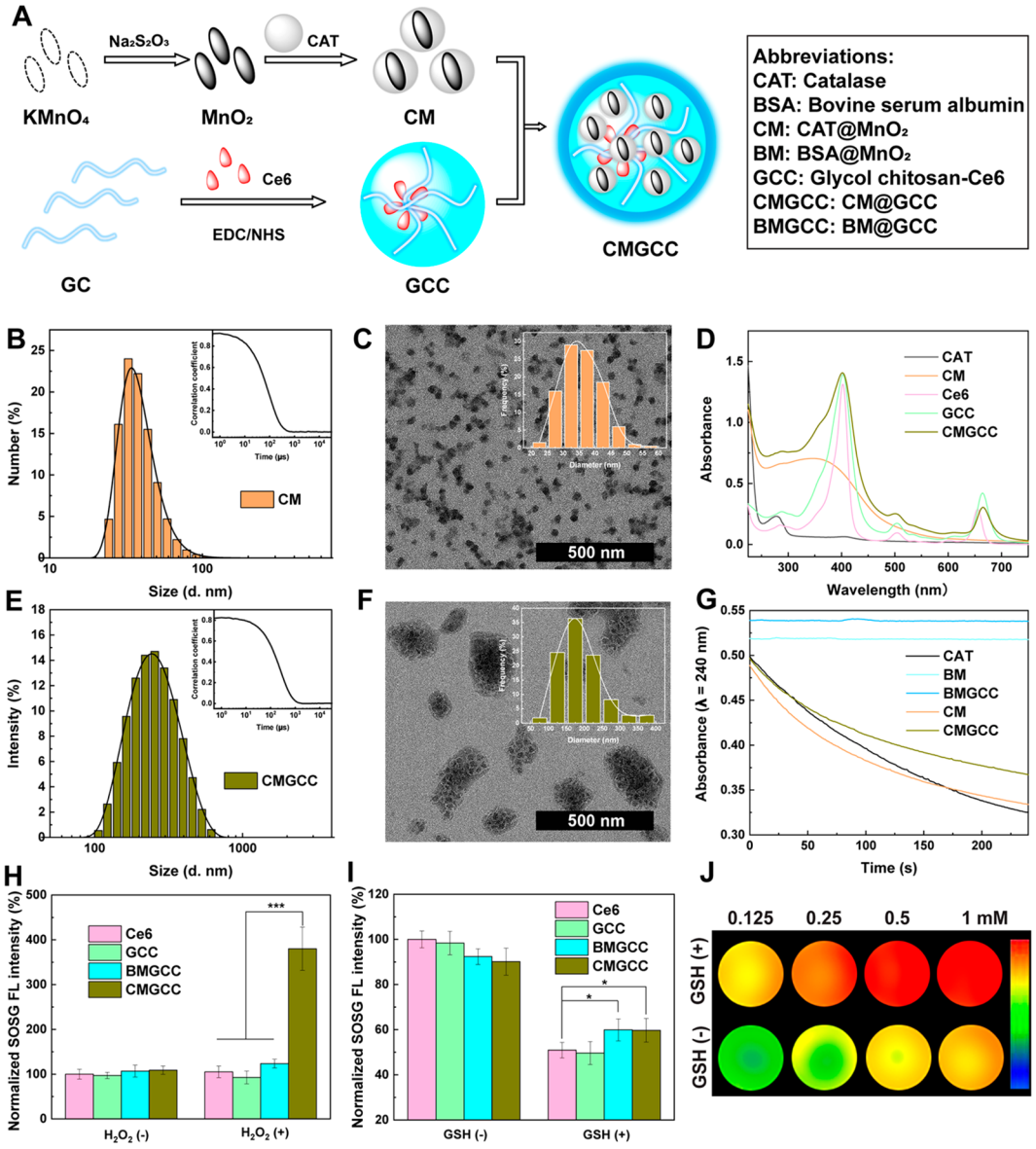

Figure 1. (A) Synthetic route for the formation of CMGCC nanoclusters. Abbreviations of the different components used are listed in the right frame. (B) Hydrodynamic size distribution and correlation coefficient (inset) of CM nanoparticles in water. (C) TEM image and size distribution histogram (inset) of CM nanoparticles. (D) UV−vis spectra of CAT, CM, Ce6, GCC, and CMGCC. (E) Hydrodynamic size distribution and correlation coefficient (inset) of CMGCC nanoclusters in water. (F) TEM image and size distribution histogram (inset) of CMGCC nanoclusters. (G) UV absorbance change of H_2O_2 solution (λ = 240 nm) incubated with CAT, BM, BMGCC, CM, and CMGCC over a period of 4 min and relative enzyme activity of CM and CMGCC. (H) Normalized fluorescence of SOSG in Ce6, GCC, BMGCC, and CMGCC solutions in the absence or presence of H_2O_2 ([Ce6] = 5 μg/mL, [SOSG] = 5 μM, [H_2O_2] = 100 μM). (I) Normalized fluorescence of SOSG in Ce6, GCC, BMGCC, and CMGCC solutions in the absence or presence of GSH ([Ce6] = 5 μg/mL, [SOSG] = 5 μM, [GSH] = 5 mM). (J) Pseudocolored T_1-weighted MR images of CMGCC with different Mn concentrations in the presence or absence of GSH (10 mM). The color bar from blue to red indicates the gradual increase of MR signal intensity.

growth inhibition by boosting PDT efficacy (Scheme 1). We rationally encapsulated CAT-stabilized MnO_2 (CM) nanoparticles within chlorin e6 (Ce6)-loaded GC (GCC) micelles to form hybrid CMGCC nanoclusters. In this system, (1) the presence of the GC polymer endows the nanoclusters with prolonged circulation time and a tumor microenvironment pH-stimulated charge switch, thereby improving the accumulation within the tumor tissue; (2) when endocytosed by the cancer cells, CAT can catalyze the conversion of endogenous H_2O_2 to generate O_2 for increasing O_2 levels in the PDT process; (3) the MnO_2 acts as an oxidizing agent to decrease the intracellular GSH to avert the reduction of the generated $^1O_2$, and the consequently produced Mn^{2+} can be employed as a T_1-weighted MRI contrast agent. We demonstrate that these synergistic multifunctional CMGCC nanoclusters with outstanding MR imaging contrast capability and prominent *in vitro* and *in vivo* PDT performance present a promising direction for future cancer therapy.

RESULTS AND DISCUSSION

Synthesis and Characterization of CM, GCC, and CMGCC. The synthetic process to construct the CMGCC nanoclusters is shown in Figure 1A: (1) MnO_2 nanoparticles were first fabricated *via* a redox reaction between $KMnO_4$ and

https://dx.doi.org/10.1021/acsnano.0c03080
ACS Nano 2020, 14, 11225−11237

excess $Na_2S_2O_3$, followed by stabilization with CAT to obtain the CM nanoparticles;[48] (2) through an *N*-(3-(dimethylamino)propyl)-*N*′-ethylcarbodiimide hydrochloride (EDC) and *N*-hydroxysuccinimide (NHS)-mediated coupling reaction, natural GC (polymerization degree ≥400, purity ≥60%) polymer was modified with Ce6 to achieve GCC micelles;[49] (3) the as-prepared CM nanoparticles and GCC micelles were mixed, sonicated, and stirred at room temperature to give the final CMGCC nanoclusters.

The formation of CM nanoparticles was characterized with a range of techniques. Dynamic light scattering (DLS) showed that the CM nanoparticles exhibited a hydrodynamic size peak of 34.4 ± 2.98 nm in water (Figure 1B) and a negative surface potential of −22.6 ± 0.50 mV (Figure S1). Transmission electron microscopy (TEM) and scanning electron microscopy (SEM) images revealed that the as-prepared CM nanoparticles displayed uniform spherical morphology and good monodispersity, with an average size of 35.8 ± 6.23 nm (measured by TEM, Figures 1C and S2), which was consistent with the DLS result. The synthesis of MnO_2 was evidenced by the ΔE of Mn_{2p} and Mn_{3s} spin−orbit of 11.8 and 4.7 eV, respectively, in the X-ray photoelectron spectroscopy spectra (Figure S3). The characteristic UV−vis absorption peaks appearing at 278 and 350−600 nm could be attributed to CAT and MnO_2, respectively (Figure 1D). The strong absorption band at 1644 and 493 cm^{-1} in the Fourier transform infrared (FTIR) spectra could be allotted to the C═N bond of CAT and the Mn−O bond of MnO_2, respectively, further validating the construction of CM nanoparticles (Figure S4). The loading percentage of MnO_2 within the CM nanoparticles was calculated to be 24.6% by inductively coupled plasma optical emission spectrometry (ICP-OES). These results therefore demonstrate the successful formation of CM nanoparticles. To investigate the role of CAT in the nanosystem, bovine serum albumin (BSA)-stabilized MnO_2 (BM) nanoparticles were synthesized for comparison, following the same protocol (Figure S5).

The synthesis of Ce6-conjugated glycol chitosan (GCC) was performed according to an earlier reported procedure.[49] The synthesis of GCC was confirmed using ^1H NMR spectroscopy (Figure S6), and the Ce6 substitution degree was determined to be 8.9 wt % with UV−vis spectroscopy. In aqueous conditions, the amphiphilic GCC self-assembled into micelles, as revealed by SEM (Figure S7). The GCC micelles exhibited a positive surface potential of 19.7 ± 0.21 mV (Figure S1) and a hydrodynamic size of 514 ± 15 nm (Figure S8).

In the next step, the CM nanoparticles were combined with the GCC micelles to form multifunctional nanoclusters (CMGCC) *via* electrostatic interactions[24] and Mn−N coordination.[50] Different mass feed ratios of CM/GCC (1:0.5, 1:1, and 1:2) were utilized to optimize the formation of CMGCC nanoclusters. It is worth noting that, with the increase of the amount of CM, the hydrodynamic size of the CMGCC compared to that of GCC micelles first decreased, possibly because of the compression of the structural softness by the solid CM nanoparticles, whereafter it slightly increased upon further CM addition (Table S1). Therefore, the feed ratio of CM/GCC was set at 1:1 to render the CMGCC NCs with the smallest hydrodynamic size of 202 ± 2 nm (Figure 1E). Correspondingly, the loading content of MnO_2 and Ce6 in the CMGCC was determined to be 12.3 and 4.5 wt %, respectively. TEM and SEM images revealed that the CM nanoparticles were homogeneously distributed within the GCC micelles to form a cluster morphology with a mean particle size of 190 nm (Figures 1F and S9). The formation of CMGCC was validated by the characteristic UV−vis absorptions (Figure 1D) at 278 nm (CAT), 300−600 nm (MnO_2), and 660 nm (Ce6) and FTIR peaks (Figure S4) at 1644 cm^{-1} (C═O), 1062 cm^{-1} (C−O−C), and 493 cm^{-1} (Mn−O). The CMGCC nanoclusters exhibited a fluorescence emission peak at of 660 nm, in line with the free Ce6 (Figure S10).[51] The hydrodynamic size change of the CMGCC nanoclusters in phosphate-buffered saline (PBS) and cell culture medium was evaluated by DLS measurement (Figures S11) over a period of 2 weeks, which demonstrated that the clusters were not affected by these different environments as the size remained constant, which is favorable for biomedical applications. For comparison, BM nanoparticles encapsulated within the GCC micelles (BMGCC) were also fabricated using the same protocol, which displayed a hydrodynamic size similar to that of the CMGCC (Figure S12). Interestingly, zeta-potentials of the CMGCC nanoclusters increased from 2.5 to 10.0 mV in PBS and from −0.1 to 7.4 mV in Dulbecco's modified Eagle medium (DMEM) containing 10% of fetal bovine serum, as the pH decreased from 7.4 to 6.5, indicating that this may contribute to enhanced accumulation of CMGCC nanoclusters in acidic tumor microenvironments.

Evaluation of CAT Activity. Following the synthesis process of the CMGCC nanoclusters, the CAT activity with respect to the decomposition of H_2O_2 into O_2 was evaluated by measuring the UV absorbance change of H_2O_2 following our previous method.[52] As shown in Figures 1G and S13A, the CAT activity of CM nanoparticles was determined to be similar to that of free CAT, indicating that the preparation of CM nanoparticles has no obvious impact on the CAT activity. The CAT activity of CMGCC nanoclusters decreased to 62% of its initial catalytic activity, which can be attributed to the fact that the introduction of the GCC polymer shell leads to steric hindrance and mass transport resistance, which hinders the access of H_2O_2 to the enzyme. Furthermore, we also observed that BM nanoparticles and BMGCC nanoclusters did not induce any obvious absorbance change under the given experimental conditions, indicating no catalytic activity toward the decomposition of H_2O_2 within the measurement period of 4 min. The CAT catalytic activity was further validated by recording the O_2 concentration change after coincubation of CAT, CM or CMGCC with an H_2O_2 solution, which indicated that the activity of both CM and CMGCC was sufficient to mediate the decomposition of H_2O_2 (Figure S13). The enzyme activity of CMGCC after longer-term storage was also studied. We found that the CMGCC nanoclusters still retained 52% of their initial activity after storage for 14 days at 4 °C. Previous studies have proven that the immobilization of CAT within a polymer shell can significantly improve the stability of CAT against proteolysis.[53,54] To verify this, free CAT and CMGCC nanoclusters were co-incubated with trypsin (44 μM) for 90 min, and the corresponding catalytic activity was recorded. The CMGCC nanoclusters retained 91% of their initial activity, indicating the favorable resistance against proteolysis. Overall, the developed CMGCC nanoclusters exhibit high enough catalytic capacity toward the production of O_2 from H_2O_2 for biomedical applications.

Singlet Oxygen Generation. The $^1O_2$ generation behavior of CMGCC nanoclusters was next assessed using singlet oxygen sensor green (SOSG). SOSG could be rapidly oxidized by $^1O_2$ to yield SOSG endoperoxides, emitting a strong green fluorescence. We first explored the impact of

https://dx.doi.org/10.1021/acsnano.0c03080
ACS Nano 2020, 14, 11225−11237

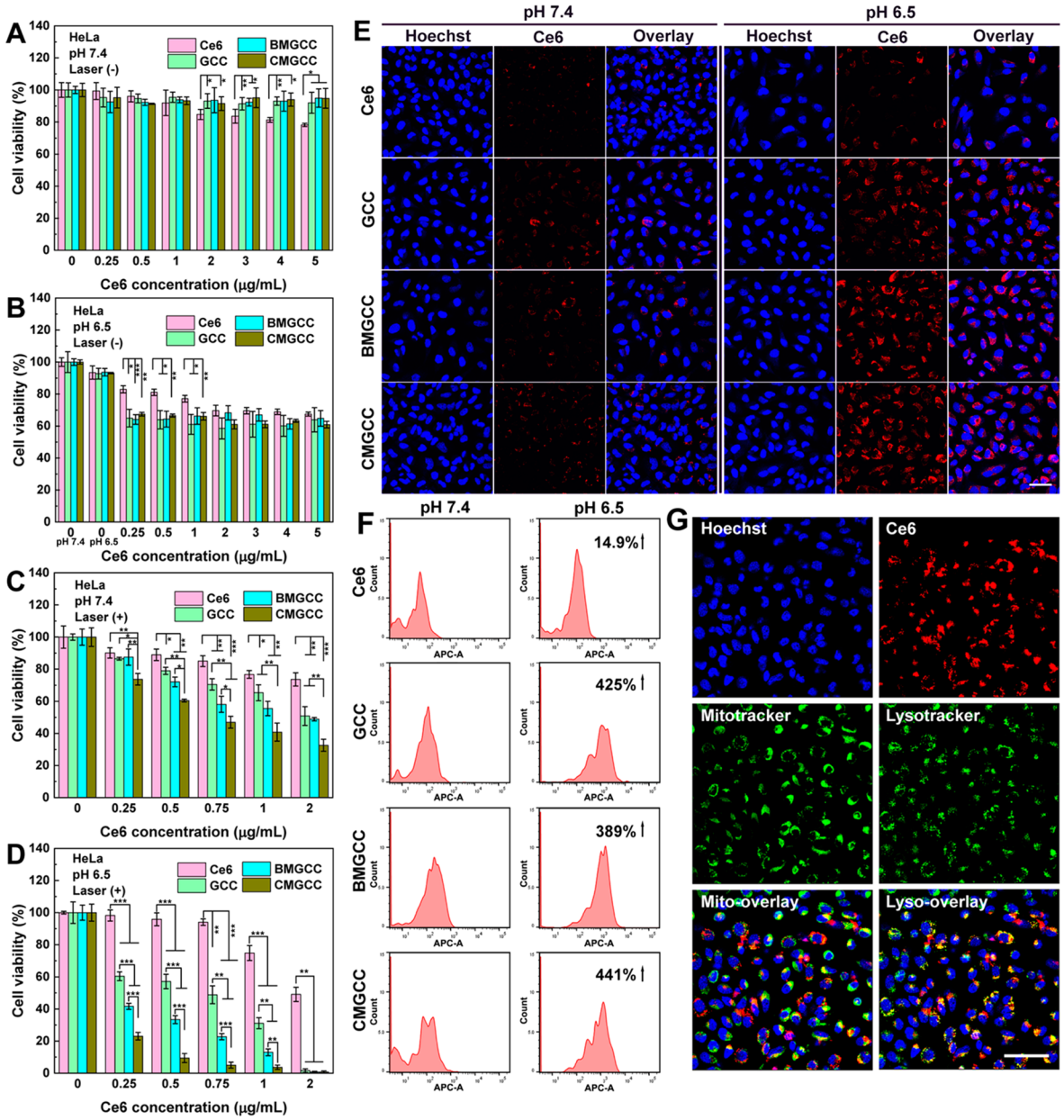

Figure 2. (A) Cell viabilities of HeLa cells treated with Ce6, GCC, BMGCC, and CMGCC at different Ce6 concentrations under physiological pH 7.4 in the absence of laser irradiation. (B) Cell viabilities of HeLa cells treated with Ce6, GCC, BMGCC, and CMGCC at different Ce6 concentrations under pH 6.5 in the absence of laser irradiation. (C) Cell viabilities of HeLa cells treated with Ce6, GCC, BMGCC, and CMGCC at different Ce6 concentrations under pH 7.4 in the presence of laser irradiation (100 mW/cm^2, 5 min). (D) Cell viabilities of HeLa cells treated with Ce6, GCC, BMGCC, and CMGCC at different Ce6 concentrations under pH 6.5 in the presence of laser irradiation (100 mW/cm^2, 5 min). (E) CLSM images of HeLa cells incubated with Ce6, GCC, BMGCC, and CMGCC ([Ce6] = 0.5 μg/mL) at pH 7.4 and 6.5. Scale bar = 50 μm. (F) Quantified FACS analysis of Ce6 fluorescence of HeLa cells treated with Ce6, GCC, BMGCC, and CMGCC ([Ce6] = 0.5 μg/mL) at pH 7.4 and 6.5. (G) CLSM images of intracellular localization of CMGCC within HeLa cells ([Ce6] = 2 μg/mL). The cell nuclei, mitochondria, and lysosomes were stained with Hoechst, Mitotracker, and Lysotracker, respectively. Scale bar = 50 μm.

hypoxia on the $^1O_2$ generation. To mimic the hypoxic tumor microenvironment, Ce6, GCC, BMGCC, and CMGCC solutions containing SOSG were first bubbled with argon for at least 45 min to remove the dissolved O_2 and then irradiated with a 660 nm laser in the presence or absence of H_2O_2 (100 μM). As can be seen from Figure 1H, the fluorescence intensity of all systems tested was similar before and after irradiation in the absence of H_2O_2, suggesting that hypoxia has a strong inhibition effect on the $^1O_2$ generation. It is worth noting that only the experiment of CMGCC in the presence of H_2O_2 showed significantly increased fluorescence intensity (4-fold higher than that of the BMGCC control group), which can be attributed to the reoxygenation *via* the CAT-mediated H_2O_2 decomposition. Next, we studied the role of GSH depletion on the $^1O_2$ generation. To achieve this, the effect of CM nanoparticles and CMGCC nanoclusters on GSH depletion was monitored *via* the UV−vis absorbance of MnO_2. It is clear from Figure S14 that the absorbance of MnO_2 in CM and CMGCC remains stable in the absence of GSH. Upon addition of 10 mM of GSH, the absorbance

https://dx.doi.org/10.1021/acsnano.0c03080
ACS Nano 2020, 14, 11225−11237

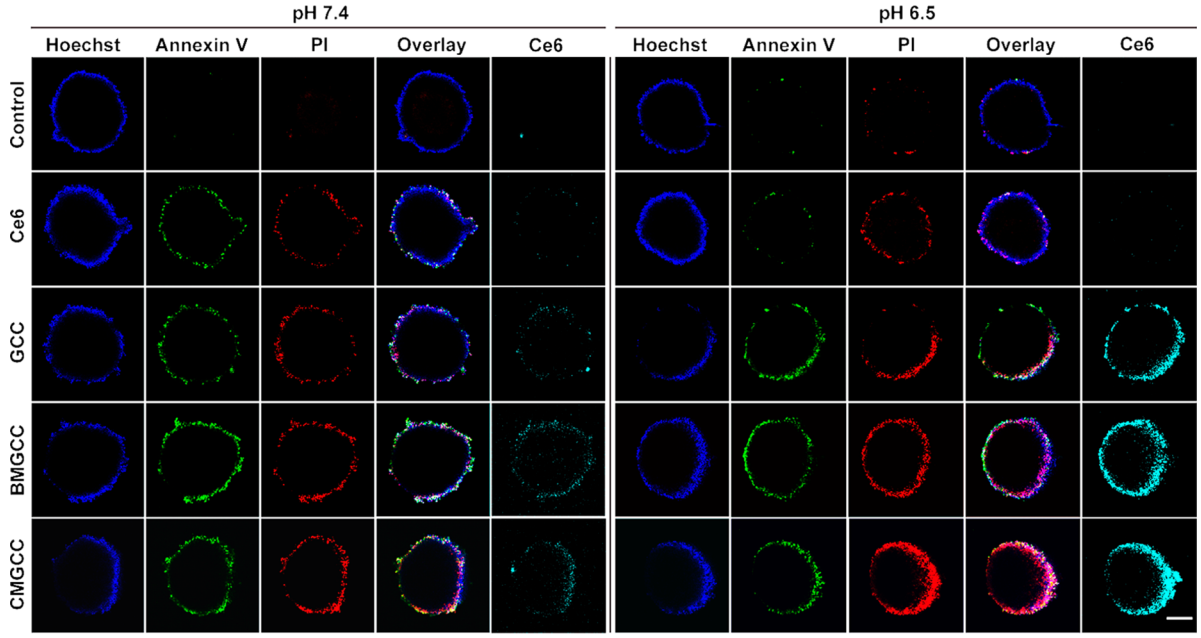

Figure 3. CLSM images of 3D MCSs after treatment with Ce6, GCC, BMGCC, and CMGCC ([Ce6] = 0.5 μg/mL) with 660 nm laser irradiation (100 mW/cm^2, 5 min) at pH 7.4 and 6.5. The cell nuclei, early apoptotic, and dead cells were stained with Hoechst, FITC-Annexin V, and PI, respectively. Scale bar = 250 μm.

disappeared within 4 min, indicating that MnO_2 immediately consumed GSH. The diminishing effect of GSH on $^1O_2$ generation was also validated using SOSG (Figure 1I), which showed that the presence of MnO_2 in both BMGCC and CMGCC nanoclusters led to an increase in $^1O_2$ generation by consuming GSH. The above SOSG assays thus demonstrated that the CMGCC nanoclusters can improve the $^1O_2$ generation efficacy *via* CAT-mediated reoxygenation, while diminishing $^1O_2$ consumption *via* MnO_2-mediated GSH decomposition.

MR Relaxometry. Mn^{2+} has been approved by the FDA as a clinical T_1-weighted MR imaging contrast agent (*e.g.*, Teslascan). The MR imaging performance of the developed CMGCC nanoclusters was next investigated. It is clear from Figure 1J that a significant concentration-dependent MR contrast enhancement was observed when the CMGCC nanoclusters were treated with 10 mM of GSH, whereas a MR enhancement trend was found to be low in the absence of GSH. The longitudinal relaxivity (r_1) value of CM and CMGCC in the absence of GSH was measured to be 0.05 and 0.03 mM^{-1} s^{-1}, respectively (Figure S15). Notably, the r_1 value of the CM and CMGCC in the presence of GSH was determined to be 9.58 and 9.19 mM^{-1} s^{-1}, respectively, which is much higher than that of clinical Gd-based contrast agent (Magnevist, r_1 = 4.56 mM^{-1} s^{-1}).[55] This indicates that the GSH-responsive CMGCC nanoclusters may function as an effective contrast agent for T_1-weighted MR imaging of tumors that have a high local concentration of GSH.

***In Vitro* Cytotoxicity and Cellular Uptake Behavior Assays.** After establishing the favorable physical features of CMGCC nanoclusters for enhanced $^1O_2$ generation and MR imaging, cell experiments were conducted to investigate *in vitro* PDT performance. The cytocompatibility of CMGCC nanoclusters toward both healthy human embryonic kidney cells 293 (HEK 293) and cancerous HeLa cells was evaluated with a standard 3-(4,5-dimethylthiazol-2-yl)-2,5-diphenyltetrazolium bromide (MTT) assay. Indeed, we observed low dark toxicity of the CMGCC nanoclusters up to a Ce6 concentration of 5 μg/mL (Figures 2A,B and S16), suggesting their encouraging cytocompatibility. Next, PDT-induced cytotoxicity *via* 660 nm laser irradiation (100 mW/cm^2 for 5 min) in both physiological pH 7.4 and tumor acidic pH 6.5 was conducted. Figure 2C,D revealed that the incubation with CMGCC nanoclusters provided the most effective PDT inhibition effect over all other groups, likely owing to the sufficient O_2 supplement[56] and GSH depletion.[10] Importantly, HeLa cell viability cultured at pH 6.5 in all cases where GCC was present was much lower than that at 7.4, which can be attributed to the surface charge switchability of the GC shell from neutral to positive, thus improving the uptake amount. It is worth noting that owing to the synergistic combination of MnO_2, CAT and the charge-switchable GC polymer, the CMGCC nanoclusters efficiently killed the cancer cells (cell viability <10%) even at a noticeably low Ce6 concentration of 0.5 μg/mL at a tumor acidic pH 6.5, which is much more effective than PDT systems reported in previous literature.[10,28,49] The half-maximal inhibitory concentration (IC_{50}) of CMGCC toward HeLa cells was determined to be 0.12 μg/mL at pH 6.5, which is significantly smaller than that at pH 7.4 (0.74 μg/mL, Figure S17). This PDT-induced apoptosis was further visualized using confocal laser scanning microscopy (CLSM) with fluorescein isothiocyanate (FITC)-Annexin V/propidium iodide (PI) staining. It is clear in Figure S18 that the HeLa cells treated with CMGCC nanoclusters at pH 6.5 showed the highest cell death, in line with the MTT results. 2′,7′-Dichlorofluorescein diacetate (DCF-DA) was next utilized as a fluorescent indicator to investigate the *in vitro* $^1O_2$ generation. DCF-DA could be hydrolyzed by the intracellular esterases and emit green fluorescence in the presence of $^1O_2$. As shown in Figure S19, the employment of GC polymer significantly improved the $^1O_2$ generation within the HeLa cells cultured at an acidic pH 6.5, possibly because of the enhanced uptake due to surface charge switchability. Treatment with CMGCC at acidic pH provided the most noticeable fluorescence intensity when compared to that in all other groups, which can be attributed

https://dx.doi.org/10.1021/acsnano.0c03080
ACS Nano 2020, 14, 11225−11237

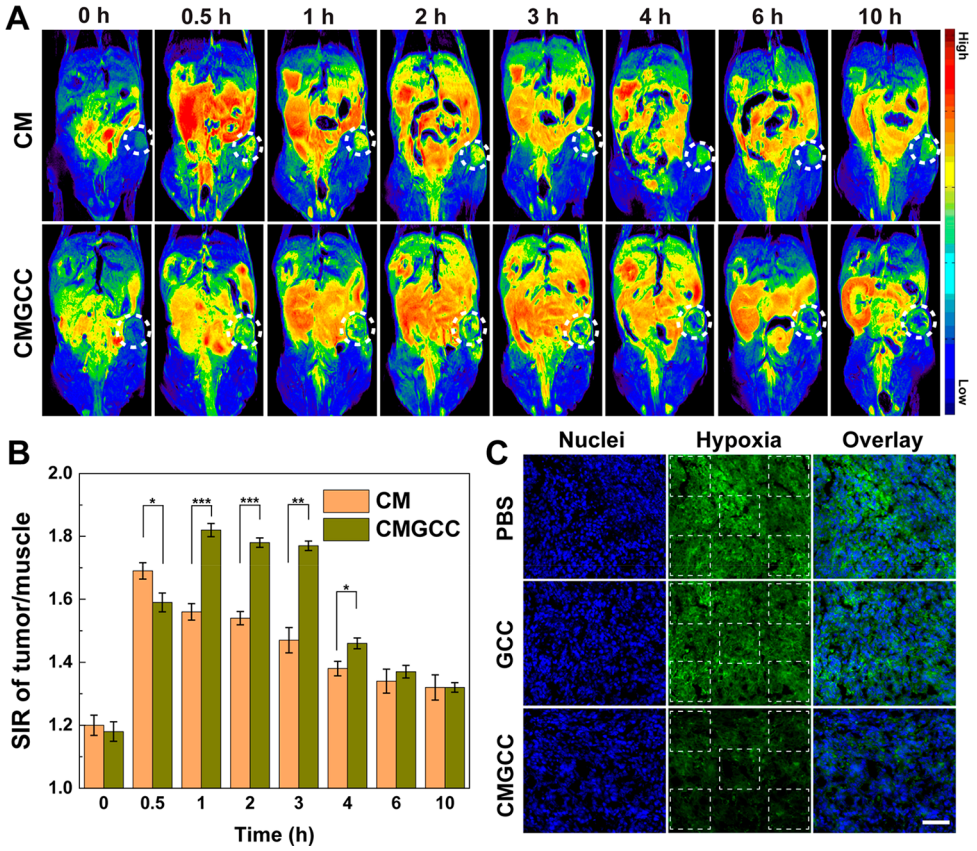

Figure 4. (A) *In vivo* pseudocolored T_1-weighted MR images of nude mice bearing xenografted HeLa tumors before and at different time points postinjection of CM and CMGCC ([MnO_2] = 4.2 mg/kg). (B) MR signal intensity ratio (SIR) analysis of the tumor region at different time points postinjection of the CM and CMGCC ([MnO_2] = 4.2 mg/kg). (C) Immunofluorescence staining images of tumor slices after different treatments. The cell nuclei and hypoxic areas were stained by DAPI (blue) and antipimonidazole antibody (green), respectively. Scale bar = 200 μm.

to the aforementioned synergistic elements. *In vitro* cytotoxicity assays therefore demonstrate that the developed CMGCC nanoclusters displayed no obvious toxicity toward both healthy and cancerous cells without laser irradiation, but meanwhile could improve the *in vitro* PDT toxicity after irradiation by taking advantage of reoxygenation, GSH depletion, and charge switchability.

The pH-induced enhanced cellular uptake was next investigated. CLSM data demonstrate that the HeLa cells treated with free Ce6 showed similar fluorescence at both pH 7.4 and 6.5, whereas the fluorescence of HeLa cells treated with GCC, BMGCC, and CMGCC nanoclusters at pH 6.5 was much higher than that at pH 7.4 (Figures 2E and S20). This uptake enhancement was further quantified using FACS (Figure 2F). CLSM and FACS studies thus indicate that HeLa cells could internalize more GCC-containing nanoparticles at the tumor-acidic pH 6.5, which could contribute to improved cancer cell killing ability. As $^1O_2$ kills cancerous cells by oxidizing the surrounding biomacromolecules such as proteins and lipids to rupture the subcellular structures (within an effective range of <0.2 μm), selective delivery of a PS to subcellular organelles can contribute to an enhanced PDT effect.[20,57] We therefore next investigated the subcellular distribution of the CMGCC nanoclusters within HeLa cells using Mitotracker and Lysotracker to label the mitochondria and lysosomes, respectively. As observed from Figure 2G, the fluorescence of Ce6 was mostly merged with that of the lysosomes, revealing that the developed CMGCC nanoclusters were able to localize into lysosomes, thus enhancing the PDT efficacy.

PDT toward 3D Tumor Multicellular Spheroid Models. 3D tumor multicellular spheroids (MCSs) have been widely utilized as cancer therapeutics screening platforms because they can better mimic the solid tumor morphology and tumor microenvironment over the monolayer-based cell cultures.[58−60] Therefore, MCSs comprising fibroblasts (NIH/3T3) and cancerous HeLa cells (NIH/3T3/HeLa = 5:1) were employed to investigate tumoral uptake behavior. Briefly, 3D MCSs were incubated with Ce6, GCC, BMGCC, and CMGCC ([Ce6] = 0.5 μg/mL) at pH 7.4 or 6.5 for 4 h and then irradiated with a 660 nm laser (100 mW/cm^2, 5 min). After a follow-up culture overnight, the MCSs were stained with FITC-Annexin V/PI and observed under CLSM. It is apparent in Figure 3 (enlarged in Figures S21 and S22) and Figure S23 that the employment of GCC significantly improved the PDT outcome under acidic pH 6.5; again, the presence of CAT and MnO_2 contributed to enhanced cell apoptosis/death, in line with the previous cytotoxicity assays. The superior PDT performance of CMGCC nanoclusters toward 3D MCSs was further evidenced by the detachment of dead cells from the MCS surface monitored with an optical microscope (Figure S24). These results thus verify that CMGCC nanoclusters are capable of enhancing PDT efficacy *via* their ability to function as a multifunctional carrier.

***In Vitro* and *In Vivo* MR Imaging.** After illustrating the *in vitro* PDT performance, we investigated the potential of the

https://dx.doi.org/10.1021/acsnano.0c03080
ACS Nano 2020, 14, 11225−11237

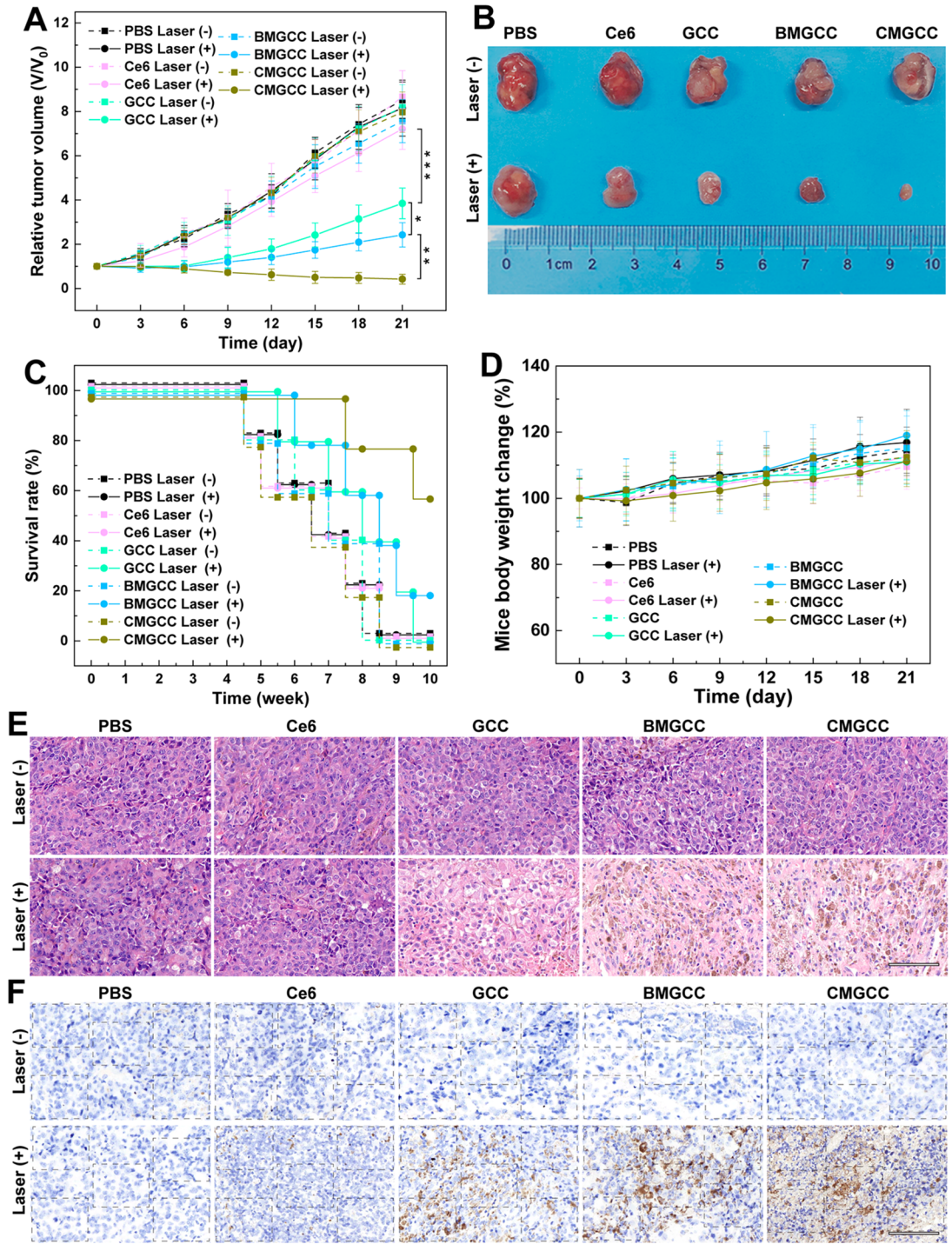

Figure 5. (A) Tumor growth curves after the different treatments (n = 6). Tumor volumes (V) were normalized to the initial values (V_0). (B) Photograph of tumors on day 21 after the *in vivo* PDT therapy. (C) Survival rate of the HeLa-tumor-bearing nude mice after different treatments (n = 5). (D) HeLa-tumor-bearing nude mice body weight changes of the different groups over 21 days. (E) H&E staining of tumor slices taken on day 21 after different treatments. Scale bar = 100 μm. (F) TUNEL staining of tumor slices taken on day 21 after different treatments (blue, live cells; brown, necrotic and apoptotic cells). Scale bar = 100 μm.

developed CMGCC nanoclusters to be utilized as a contrast agent for T_1-weighted MR imaging. HeLa cells were incubated with the CMGCC nanoclusters at different Mn concentrations under culture at pH 7.4 and 6.5 for 4 h, and *in vitro* MR imaging was performed. We can see from Figure S25 that the CMGCC nanoclusters increased the MR signal intensity of HeLa cells with Mn concentration. Importantly, at an acidic culture pH of 6.5, a higher signal intensity was detected, probably due to improved endocytosis, in line with the uptake assays. To further explore the *in vivo* imaging performance, pseudocolored T_1-weighted MR images and the corresponding signal intensity ratio (SIR) were recorded at different time intervals after i.v. injection in mice of CM and CMGCC ([MnO_2] = 4.2 mg/kg) through the tail vein. It is apparent from Figure 4A that the tumor site showed a low MR signal before the injection but started to be lightened up post-

https://dx.doi.org/10.1021/acsnano.0c03080
ACS Nano 2020, 14, 11225−11237

injection of both the CM nanoparticles and CMGCC nanoclusters. The MR signal of the tumor region rose to the highest value at 0.5 h postinjection of the CM nanoparticles and then started to decrease. Notably, this inflection point for the CMGCC nanocluster treatment was 1 h, longer than that of CM treatment. This can be attributed to (1) the relatively smaller size of CM nanoparticles, which contributes to faster clearance;[21] and (2) the employment of GCC, which possesses abundant hydroxyl groups, which could prolong the *in vivo* circulation time.[23] The injection of CMGCC nanoclusters yielded a higher contrast enhancement compared to the treatment of CM nanoparticles (Figure 4B), which can be attributed to improved internalization as a result of the charge switchability under mild acidic conditions experienced in the tumor microenvironment. Therefore, MR imaging results reveal that the developed CMGCC nanoclusters on the one hand display efficient tumor homing ability *via* the enhanced permeability and retention effect and charge switchability and on the other hand could produce Mn^{2+} ions upon reduction by the endogenous GSH for effective tumor MR imaging.

***In Vivo* PDT.** Encouraged by the effective *in vitro* PDT performance and effective tumor MR imaging ability, we evaluated *in vivo* PDT efficacy using nude mice bearing HeLa tumors. First, a hypoxia immunofluorescence assay was employed to examine the ability of the CMGCC nanoclusters to ameliorate the tumor hypoxic status. As can be seen from Figures 4C and S26, large hypoxic areas were observed in the groups of control and GCC treatment, whereas the hypoxic areas in the group of CMGCC treatment were significantly reduced, indicating that the CAT-mediated decomposition of H_2O_2 into O_2 was able to relieve the tumor hypoxia. For the *in vivo* PDT, the nude mice were randomly divided into 10 groups: PBS (control), Ce6, GCC nanoparticles, BMGCC nanoclusters, and CMGCC nanoclusters, each in the presence and absence of laser irradiation, 6 mice per group, with a corresponding Ce6 dose of 1.5 mg/kg. For the laser irradiation group, the mice were subjected to laser irradiation (660 nm, 100 mW/cm^2, 10 min) 3 h after i.v. injection, which is based on the *in vivo* MR imaging results that the high MR signal of the tumor site occurred within the first 3 h, indicated the high accumulation of CMGCC nanoclusters. The therapeutic performance was assessed by recording the tumor volume changes. Figure 5A reveals that the control group and all groups in the absence of laser irradiation exhibited a similar unperturbed tumor growth. The Ce6 group in the presence of laser irradiation showed no obvious tumor growth inhibition effect due to the fast clearance of the small drug. Interestingly, the GCC nanoparticle treatment in the presence of irradiation provided a noticeable tumor suppression effect over the Ce6 treatment, which can be attributed to the charge switchability of the GC polymer within the tumor acidic microenvironment, which improved the internalization of the PS, thus leading to more $^1O_2$ generation to kill the cancer cells. The BMGCC nanocluster treatment in the presence of irradiation further inhibited the tumor growth, compared to the GCC treatment, which can be attributed to the MnO_2-mediated GSH depletion, which sensitizes the cancer cells to the $^1O_2$. Most importantly, the CMGCC nanocluster treatment offered the most noticeable tumor suppression over all other groups, which can be attributed to the synergistic elements of (1) the GC polymer for enhanced accumulation, (2) MnO_2 for GSH depletion, and (3) CAT for reoxygenation. At the end of the *in vivo* PDT therapy (day 21), one representative tumor from each group was harvested, photographed, and sent for hematoxylin/eosin (H&E) and TdT-mediated dUTP nick-end labeling (TUNEL) staining to validate the therapeutic effect. The other five mice from each group were further fed to determine the survival rate. It is clear from Figure 5B that the tumor in the group of CMGCC nanocluster treatment in the presence of laser irradiation was the smallest among all of the groups. Importantly, the CMGCC nanocluster treatment with laser irradiation significantly improved the survival rate even after 10 weeks (Figure 5C). The H&E and TUNEL staining also revealed that the group of CMGCC nanocluster treatment displayed the highest necrosis and apoptosis ratio among all groups, consistent with tumor growth results (Figures 5E,F and S27). The *in vivo* PDT results thus reveal that the CMGCC nanoclusters developed exhibit a dramatically improved PDT efficacy toward subcutaneous HeLa tumors.

***In Vivo* Pharmacokinetics and Biodistribution.** The *in vivo* pharmacokinetics and biodistribution of the developed CMGCC NCs were further investigated. The blood circulation profile was studied by tracking the Mn content in blood at different time intervals after i.v. injection of the CMGCC nanoclusters into healthy mice. We can see from Figure S28 that the Mn blood levels decreased over time following a two-compartment model, with a first ($t_{1/2}$ (α)) and second ($t_{1/2}$ (β)) phase of circulation half-lives of 1.23 and 6.87 h, respectively, determined by a secondary exponential fitting. This moderately long circulation time of CMGCC nanoclusters in blood could contribute to effective tumor accumulation, which was further confirmed by a relatively high ID%/g of 8.36 within the tumor tissue at 24 h postinjection by measuring the Mn content using ICP-OES (Figure S29). The *in vivo* biodistribution of the CMGCC nanoclusters in the major organs including heart, liver, spleen, lung, and kidney was next quantified to explore their metabolism behavior using healthy mice. Notably, a significantly high level of Mn in the liver and kidney was observed (Figure S30), which implies two possible metabolic pathways of CMGCC nanoclusters: (1) macrophage clearance by the reticuloendothelial system and (2) renal clearance of the Mn^{2+} ions generated from MnO_2 decomposition. Notably, after 7 days, the retention of Mn in the major organs decreased to a low level, suggesting an efficient clearance of CMGCC nanoclusters from the mouse body, which is of great importance for *in vivo* applications.

***In Vivo* Biocompatibility Evaluation.** Hemolysis assays and blood routine tests were performed to study the hemocompatibility of the developed CMGCC nanoclusters. We can see from hemolysis results (Figure S31) that the hemolysis percentage is less than 3% at the studied CMGCC concentrations, indicating their favorable hemocompatibility. The blood routine analysis results revealed that injection of CMGCC nanoclusters did not affect nine routine parameters, indicating negligible blood toxicity (Table S2). To estimate the *in vivo* toxicity of CMGCC nanoclusters, the body weight change of HeLa-tumor-bearing nude mice in all groups following the *in vivo* PDT process was recorded. It is clear from Figure 5D that no obvious body weight change was observed in all groups following the process of *in vivo* therapy. H&E staining of the major organs of HeLa-tumor-bearing nude mice on day 21 postinjection of CMGCC nanoclusters further exhibited that no significant pathological abnormalities such as inflammatory infiltrate, morphological changes, and necrosis were observed (Figure S32), implying the satisfactory

https://dx.doi.org/10.1021/acsnano.0c03080
ACS Nano 2020, 14, 11225−11237

biocompatibility to the mice organs. In particular, one safety concern for Mn-based nanoplatforms is that excessive exposure to a high dose of Mn is associated with adverse neurotoxicity, which may induce poor cognitive performance similar to the Parkinsonian syndromes. Therefore, the brain Mn content and pathological condition were investigated after the intravenous injection of the developed CMGCC. As can be seen in Figure S30, negligible Mn^{2+} was retained within the brain site. In addition, no obvious histological damage was observed in the H&E staining (Figure S32). These results indicate that the CMGCC could not permeate the blood−brain barrier, thus guaranteeing the functioning of the brain. Therefore, it is reasonable to conclude that the CMGCC nanoclusters exert the therapeutic effect *in vivo* against HeLa tumors without any significant systemic toxicity.

CONCLUSION

In summary, we have successfully developed multifunctional synergistic CMGCC nanoclusters with three features to improve PDT. The Ce6−glycol chitosan polymer conjugate afforded not only long blood circulation at physiological but also pH enhanced accumulation in the tumor site as a result of more effective cell uptake due to an increase in positive charge; the enzyme CAT contributed to reoxygenating the hypoxic tumor tissue by decomposition of endogenous H_2O_2 in O_2; and MnO_2 contributed to lowering the intracellular GSH and simultaneously enabled T_1-weighted MR imaging. Systemic administration of the CMGCC nanoclusters exhibited significantly enhanced tumor growth inhibition toward a subcutaneous HeLa tumor but with no appreciable toxic side effect. Therefore, we think that the present CMGCC nanoclusters are a promising theranostic agent for PDT, while contributing to the development of synergistic strategies for cancer treatment.

EXPERIMENTAL METHODS

Synthesis of CAT-Stabilized MnO_2 (CM) Nanoparticles. Twenty milliliters of $Na_2S_2O_3{\cdot}5H_2O$ solution (1.875 mM) was dropwise added into 10 mL of $KMnO_4$ solution (5 mM) with a constant pump rate of 1 mL/min. The mixture was allowed to stir at room temperature (RT) for 30 min. 7.5 mL of CAT solution (1.67 mg/mL) was then dropwise added into the above solution to protect the MnO_2 nanoparticles from aggregation. After stirring at RT for another 30 min, the brown solution was dialyzed against MQ water (MWCO = 1000 kDa) for 3 days at 4 °C to remove residual electrolytes and free CAT. The mixture was filtered with Ultrafree-CL centrifugal filter (0.1 μm pore size) to remove large aggregates and subsequently concentrated using an Amicon tube (MWCO = 50 kDa) to give the final CM nanoparticles. A fraction of the CM solution was subjected to freeze-drying to calculate the mass concentration and the remainder was stored at 4 °C. BSAstabilized MnO_2 (BM) nanoparticles were synthesized as a control using the same method.

Synthesis of Ce6-Conjugated Glycol Chitosan (GCC). Glycol chitosan (221 mg) was dissolved into 80 mL of MQ water and stirred overnight to obtain a clear solution. Next, 22.1 mg of Ce6 (10 wt % of GC) was dissolved into 5 mL of DMSO, and 14.2 mg of EDC and 8.5 mg of NHS were added to activate the carboxyl group of Ce6. After being stirred at RT under light protection for 2 h, the activated Ce6 was then dropwise added into the GC solution and the reaction was allowed to stir for 4 h under light protection. The mixture was dialyzed against methanol/MQ (1:1) for 1 day and MQ for another 2 days. The product was then filtered through an Acrodisc syringe filter (0.8 μm) to remove large particles and concentrated with an Amicon tube (MWCO = 50 kDa). A fraction of the GCC sample was lyophilized to determine the mass concentration and for ^1H NMR analysis. The Ce6 substitution degree in GCC was determined by measuring its UV absorbance at 660 nm, which was calibrated using a standard curve of free Ce6.

Preparation of CMGCC Nanoclusters. One milliliter of the as-prepared CM solution (3 mg/mL, MQ) was added into GCC solutions (4 mg/mL, MQ) with different feed mass ratios of 1:0.5, 1:1, and 1:2 to optimize the formation of the nanoclusters. The mixture was immediately subjected to sonication for 10 min (in an ice bath to protect the enzyme from high temperatures) and stirred at RT for another 30 min to obtain stable CMGCC nanoclusters. A small portion of CMGCC was lyophilized for characterization. For biomedical applications, dialysis using Amicon tubes (MWCO = 50 kDa) was employed for the buffer exchange.

Enzyme Activity Evaluation. The enzyme activities of catalyzing H_2O_2 to generate O_2 were determined by recording the decomposition of H_2O_2 using the UV absorbance of 240 nm.[52] Briefly, the H_2O_2 solution was diluted with PBS to give an A_{240} between 0.52 and 0.55. Native CAT, CM, BM, BMGCC, CM, and CMGCC samples were diluted with PBS to reach a CAT concentration of 50 μg/mL for each sample. Next, 2.9 mL of the prepared H_2O_2 solution and 0.1 mL of CAT-containing solution were mixed into a quartz cuvette by inversion. The UV absorbance at 240 nm was instantly monitored for 4 min. The relative enzyme activity of CM and CMGCC compared to that of native CAT was determined by recording the time required for the A_{240} to decrease from 0.45 to 0.40. Each sample was performed in triplicate. To explore the catalytic activity in the presence of protease, CAT and CMGCC were treated with trypsin (44 μM) at 37 °C for 1.5 h, and the CAT activity was then quantified as mentioned above. The O_2 concentration change in the H_2O_2 solution (500 μM) incubated with native CAT, CM, or CMGCC was monitored with a portable oxygen meter.

Singlet Oxygen Detection. SOSG was employed to evaluate the singlet oxygen generation. In brief, SOSG was mixed with free Ce6, GCC, BMGCC, or CMGCC samples ([Ce6] = 5 μg/mL, [SOSG] = 5 μM), and the mixture was irradiated with a 660 nm laser (100 mW/cm^2, 5 min). The generated $^1O_2$ was determined by recording the SOSG fluorescence intensity with an excitation/emission of 504/525 nm. The fluorescence intensity of SOSG incubated with Ce6 was normalized to be 100%. To create hypoxic conditions, all solutions were first bubbled with argon for at least 45 min to remove oxygen, and the irradiation process was conducted under an argon atmosphere. H_2O_2 (final concentration of 100 μM) and GSH (final concentration of 5 mM) were employed to imitate the tumor microenvironment.

MR Relaxometry. The CMGCC solution was diluted to different Mn concentrations (0.125, 0.25, 0.5, and 1 mM) and incubated for 1 h in the presence or absence of 10 mM of GSH. T_1 MR relaxometry was conducted on a 0.5 T NMI20 analyzing and imaging instrument. The parameters were set as follows: TR = 400 ms, TE = 20 ms, resolution = 156 mm × 156 mm, and section thickness = 0.5 mm. The r_1 relaxivity value was calculated *via* linear fitting of the inverse T_1 relaxation time as a function of Mn concentration. The pseudocolored T_1-weighted MR images of the above solutions were recorded on a 3.0 T MR imaging system (Ingenia 3.0T, Phillips, Netherlands) with the following parameters: TR = 600 ms, TE = 20 ms, NSA = 4.00, matrix = 152 × 247, slice gap = 0.5 mm, voxel = 0.2 × 0.2 × 1 mm, and FOV = 30 × 50 × 18 mm.

3D MCS Tumor Model. 3D MCS tumor models were developed by co-incubating NIH/3T3 and HeLa (5:1) cells, referring to previous literature with slight modifications.[60] Briefly, 150 mg of agarose was dispersed in 10 mL of DMEM (1.5 wt %/vol) in a conical flask. The flask was sealed with foil and subjected to autoclaving (120 °C, 20 min). The sterile agarose solution was then pipetted into a 96-well plate under aseptic conditions to give a concave surface *via* the solidification of the agarose. Then, 200 μL of NIH/3T3 and 4T1 cells mixture was seeded into the as-prepared 96-well plate at a density of 6 × 10^4 cells/mL, and the cells were incubated for 4 days to achieve the MCSs. To investigate the *in vitro* PDT performance toward the 3D MCSs, the above developed MCSs were indicated with free Ce6, GCC, BMGCC, or CMGCC ([Ce6] = 0.5 μg/mL) under both

https://dx.doi.org/10.1021/acsnano.0c03080
ACS Nano 2020, 14, 11225−11237

physiological pH 7.4 and tumor microenvironment pH 6.5 for 4 h. Laser irradiation was then carried out (100 mW/cm^2, 5 min), and the MCSs were further cultured for another 20 h. The processed MCSs were either stained with Hoechst, FITC-Annexin V, and PI for CLSM observation or monitored by optical microscopy over 2 days.

***In Vivo* MR Imaging.** HeLa-tumor-bearing nude mice were employed to investigate the MR imaging of tumor after tail-vein i.v. injection (200 μL, [MnO_2] = 4.2 mg/kg). T_1-weighted MR images were obtained at different time points (0.5, 1, 2, 3, 4, 6, and 10 h) postinjection on a 3.0 T MR imaging system (Ingenia 3.0T, Phillips, Netherlands) with the following parameters: TR = 600 ms, TE = 20 ms, NSA = 4.00, matrix = 152 × 247, slice gap = 0.5 mm, voxel = 0.2 × 0.2 × 1 mm, and FOV = 30 × 50 × 18 mm. Pentobarbital sodium (40 mg/kg) was intraperitoneally injected to the nude mice, and anesthetized mice were fixed within the custom-built rodent receiver coil during the MR imaging process. The MR signal intensity was determined using Philips DICOM viewer software, and three slices at each time point were measured. The MR intensity of tumor and hindlimb muscles was detected to calculate the SIR.

***In Vivo* PDT.** HeLa-tumor-bearing nude mice were randomly divided into 10 groups (6 for each group), which were treated with (1) PBS laser (−), (2) PBS laser (+), (3) Ce6 laser (−), (4) Ce6 laser (+), (5) GCC laser (−), (6) GCC laser (+), (7) BMGCC laser (−), (8) BMGCC laser (+), (9) CMGCC laser (−), and (10) PBS laser (+) with the corresponding MnO_2 and Ce6 dose of 4.2 and 1.5 mg/kg, respectively. Briefly, different samples (200 μL) were i.v. injected into nude mice *via* the tail vein. After 3 h, groups of 2, 4, 6, 8, and 10 received laser irradiation (660 nm, 100 mW/cm^2, 10 min). The tumor volume ($V = 1/2a \times b^2$, where a represents the tumor length and b the tumor width) and body weight were monitored every 3 days. On day 21, one representative mouse from each group was sacrificed to investigate the tumor pathological changes with H&E and TUNEL staining. The major organs including heart, liver, spleen, lung, kidney, and brain were obtained for H&E staining to evaluate the biocompatibility. The other five mice from each group were further fed to determine the survival rate.

Statistical Analysis. A Student's t test was employed for statistical analysis. The data were marked with * for $p < 0.05$, ** for $p < 0.01$, and *** for $p < 0.001$. All experimental data are displayed as the mean ± standard deviation ($n \geq 3$).

ASSOCIATED CONTENT

Supporting Information

The Supporting Information is available free of charge at https://pubs.acs.org/doi/10.1021/acsnano.0c03080.

Materials, instruments, additional experimental methods, DLS and zeta-potential measurements, TEM and SEM images, XPS spectra, FTIR spectra, ^{1}H NMR spectra, fluorescence emission spectrum, enzyme activity and O_2 generation test, UV−vis absorbance of MnO_2, MR relaxometry, cell viabilities on HEK 293 cells, CLSM images of FITC-Annexin V/PI staining, intracellular $^1O_2$ generation, optical images of 3D MCSs, T_1-weighted MR images of HeLa cells, blood circulation profile, *in vivo* biodistribution behaviors, hemolysis assay, blood routine test, and H&E staining results (PDF)

AUTHOR INFORMATION

Corresponding Authors

Xiangyang Shi − *State Key Laboratory for Modification of Chemical Fibers and Polymer Materials, International Joint Laboratory for Advanced Fiber and Low-dimension Materials, College of Chemistry, Chemical Engineering and Biotechnology, Donghua University, Shanghai 201620, People's Republic of China;* orcid.org/0000-0001-6785-6645; Email: xshi@dhu.edu.cn

Jan C. M. van Hest − *Bio-Organic Chemistry, Institute for Complex Molecular Systems, Eindhoven University of Technology, 5600 MB Eindhoven, The Netherlands;* orcid.org/0000-0001-7973-2404; Email: j.c.m.v.hest@tue.nl

Authors

Jianzhi Zhu − *Bio-Organic Chemistry, Institute for Complex Molecular Systems, Eindhoven University of Technology, 5600 MB Eindhoven, The Netherlands; State Key Laboratory for Modification of Chemical Fibers and Polymer Materials, International Joint Laboratory for Advanced Fiber and Low-dimension Materials, College of Chemistry, Chemical Engineering and Biotechnology, Donghua University, Shanghai 201620, People's Republic of China*

Tingting Xiao − *State Key Laboratory for Modification of Chemical Fibers and Polymer Materials, International Joint Laboratory for Advanced Fiber and Low-dimension Materials, College of Chemistry, Chemical Engineering and Biotechnology, Donghua University, Shanghai 201620, People's Republic of China*

Jiulong Zhang − *Department of Radiology, Shanghai Public Health Clinical Center, Fudan University, Shanghai 201508, People's Republic of China*

Hailong Che − *Bio-Organic Chemistry, Institute for Complex Molecular Systems, Eindhoven University of Technology, 5600 MB Eindhoven, The Netherlands*

Yuxin Shi − *Department of Radiology, Shanghai Public Health Clinical Center, Fudan University, Shanghai 201508, People's Republic of China*

Complete contact information is available at: https://pubs.acs.org/10.1021/acsnano.0c03080

Author Contributions

#J.Z. and T.X. contributed equally to this work.

Notes

The authors declare no competing financial interest.

ACKNOWLEDGMENTS

This study was financially supported by The Netherlands Ministry of Education, Culture and Science (Gravitation Program 024.001.035), the National Natural Science Foundation of China (81761148028), and Shanghai Education Commission through the Shanghai Leading Talents Program. J.Z. thanks the support from the China Scholarship Council.

REFERENCES

(1) Dolmans, D. E. J. G. J.; Fukumura, D.; Jain, R. K. Photodynamic Therapy for Cancer. *Nat. Rev. Cancer* **2003**, *3*, 380.

(2) Agostinis, P.; Berg, K.; Cengel, K. A.; Foster, T. H.; Girotti, A. W.; Gollnick, S. O.; Hahn, S. M.; Hamblin, M. R.; Juzeniene, A.; Kessel, D.; Korbelik, M.; Moan, J.; Mroz, P.; Nowis, D.; Piette, J.; Wilson, B. C.; Golab, J. Photodynamic Therapy of Cancer: An Update. *Ca-Cancer J. Clin.* **2011**, *61*, 250−281.

(3) Trachootham, D.; Alexandre, J.; Huang, P. Targeting Cancer Cells by ROS-Mediated Mechanisms: A Radical Therapeutic Approach. *Nat. Rev. Drug Discovery* **2009**, *8*, 579−591.

(4) Lismont, M.; Dreesen, L.; Wuttke, S. Metal-Organic Framework Nanoparticles in Photodynamic Therapy: Current Status and Perspectives. *Adv. Funct. Mater.* **2017**, *27*, 1606314.

(5) Kamkaew, A.; Chen, F.; Zhan, Y.; Majewski, R. L.; Cai, W. Scintillating Nanoparticles as Energy Mediators for Enhanced Photodynamic Therapy. *ACS Nano* **2016**, *10*, 3918−3935.

(6) Chen, H.; Qiu, Y.; Ding, D.; Lin, H.; Sun, W.; Wang, G.; Huang, W.; Zhang, W.; Lee, D.; Liu, G.; Xie, J.; Chen, X. Gadolinium-Encapsulated Graphene Carbon Nanotheranostics for Imaging-Guided Photodynamic Therapy. *Adv. Mater.* **2018**, *30*, 1802748.
(7) Liu, K.; Xing, R.; Zou, Q.; Ma, G.; Mohwald, H.; Yan, X. Simple Peptide-Tuned Self-Assembly of Photosensitizers towards Anticancer Photodynamic Therapy. *Angew. Chem., Int. Ed.* **2016**, *55*, 3036−3039.
(8) Wang, Y.; Wei, G.; Zhang, X.; Xu, F.; Xiong, X.; Zhou, S. A Step-By-Step Multiple Stimuli-Responsive Nanoplatform for Enhancing Combined Chemo-Photodynamic Therapy. *Adv. Mater.* **2017**, *29*, 1605357.
(9) Li, H.; Zhao, Y.; Jia, Y.; Qu, C.; Li, J. Covalently Assembled Dopamine Nanoparticle as an Intrinsic Photosensitizer and pH-Responsive Nanocarrier for Potential Application in Anticancer Therapy. *Chem. Commun.* **2019**, *55*, 15057−15060.
(10) Fan, H.; Yan, G.; Zhao, Z.; Hu, X.; Zhang, W.; Liu, H.; Fu, X.; Fu, T.; Zhang, X.; Tan, W. A Smart Photosensitizer-Manganese Dioxide Nanosystem for Enhanced Photodynamic Therapy by Reducing Glutathione Levels in Cancer Cells. *Angew. Chem., Int. Ed.* **2016**, *55*, 5477−5482.
(11) Lucky, S. S.; Soo, K. C.; Zhang, Y. Nanoparticles in Photodynamic Therapy. *Chem. Rev.* **2015**, *115*, 1990−2042.
(12) Dai, L.; Li, K.; Li, M.; Zhao, X.; Luo, Z.; Lu, L.; Luo, Y.; Cai, K. Size/Charge Changeable Acidity-Responsive Micelleplex for Photodynamic-Improved PD-L1 Immunotherapy with Enhanced Tumor Penetration. *Adv. Funct. Mater.* **2018**, *28*, 1707249.
(13) Zhou, J.; Li, T.; Zhang, C.; Xiao, J.; Cui, D.; Cheng, Y. Charge-Switchable Nanocapsules with Multistage pH-Responsive Behaviours for Enhanced Tumour-Targeted Chemo/Photodynamic Therapy Guided by NIR/MR Imaging. *Nanoscale* **2018**, *10*, 9707−9719.
(14) Xue, X.; Huang, Y.; Bo, R.; Jia, B.; Wu, H.; Yuan, Y.; Wang, Z.; Ma, Z.; Jing, D.; Xu, X.; Yu, W.; Lin, T.; Li, Y. Trojan Horse Nanotheranostics with Dual Transformability and Multifunctionality for Highly Effective Cancer Treatment. *Nat. Commun.* **2018**, *9*, 3653.
(15) Deng, W.; Wu, Q.; Sun, P.; Yuan, P.; Lu, X.; Fan, Q.; Huang, W. Zwitterionic Diketopyrrolopyrrole for Fluorescence/Photoacoustic Imaging Guided Photodynamic/Photothermal Therapy. *Polym. Chem.* **2018**, *9*, 2805−2812.
(16) Wang, H.; Han, X.; Dong, Z.; Xu, J.; Wang, J.; Liu, Z. Hyaluronidase with pH-Responsive Dextran Modification as an Adjuvant Nanomedicine for Enhanced Photodynamic-Immunotherapy of Cancer. *Adv. Funct. Mater.* **2019**, *29*, 1902440.
(17) Ni, K.; Lan, G.; Veroneau, S. S.; Duan, X.; Song, Y.; Lin, W. Nanoscale Metal-Organic Frameworks for Mitochondria-Targeted Radiotherapy-Radiodynamic Therapy. *Nat. Commun.* **2018**, *9*, 4321.
(18) Chakrabortty, S.; Agrawalla, B. K.; Stumper, A.; Vegi, N. M.; Fischer, S.; Reichardt, C.; Kögler, M.; Dietzek, B.; Feuring-Buske, M.; Buske, C.; Rau, S.; Weil, T. Mitochondria Targeted Protein-Ruthenium Photosensitizer for Efficient Photodynamic Applications. *J. Am. Chem. Soc.* **2017**, *139*, 2512−2519.
(19) Liu, Z.; Zou, H.; Zhao, Z.; Zhang, P.; Shan, G.; Kwok, R. T. K.; Lam, J. W. Y.; Zheng, L.; Tang, B. Tuning Organelle Specificity and Photodynamic Therapy Efficiency by Molecular Function Design. *ACS Nano* **2019**, *13*, 11283−11293.
(20) Roy, I.; Bobbala, S.; Young, R. M.; Beldjoudi, Y.; Nguyen, M. T.; Cetin, M. M.; Cooper, J. A.; Allen, S.; Anamimoghadam, O.; Scott, E. A.; Wasielewski, M. R.; Stoddart, J. F. A Supramolecular Approach for Modulated Photoprotection, Lysosomal Delivery, and Photodynamic Activity of a Photosensitizer. *J. Am. Chem. Soc.* **2019**, *141*, 12296−12304.
(21) Blanco, E.; Shen, H.; Ferrari, M. Principles of Nanoparticle Design for Overcoming Biological Barriers to Drug Delivery. *Nat. Biotechnol.* **2015**, *33*, 941.
(22) Kocak, G.; Tuncer, C.; Bütün, V. pH-Responsive Polymers. *Polym. Chem.* **2017**, *8*, 144−176.
(23) Crayton, S. H.; Tsourkas, A. pH-Titratable Superparamagnetic Iron Oxide for Improved Nanoparticle Accumulation in Acidic Tumor Microenvironments. *ACS Nano* **2011**, *5*, 9592−9601.
(24) Wang, X.; Niu, D.; Li, P.; Wu, Q.; Bo, X.; Liu, B.; Bao, S.; Su, T.; Xu, H.; Wang, Q. Dual-Enzyme-Loaded Multifunctional Hybrid Nanogel System for Pathological Responsive Ultrasound Imaging and T_2-Weighted Magnetic Resonance Imaging. *ACS Nano* **2015**, *9*, 5646−5656.
(25) Nwe, K.; Huang, C.; Tsourkas, A. Gd-Labeled Glycol Chitosan as a pH-Responsive Magnetic Resonance Imaging Agent for Detecting Acidic Tumor Microenvironments. *J. Med. Chem.* **2013**, *56*, 7862−7869.
(26) Yoon, H. Y.; Son, S.; Lee, S. J.; You, D. G.; Yhee, J. Y.; Park, J. H.; Swierczewska, M.; Lee, S.; Kwon, I. C.; Kim, S. H.; Kim, K.; Pomper, M. G. Glycol Chitosan Nanoparticles as Specialized Cancer Therapeutic Vehicles: Sequential Delivery of Doxorubicin and Bcl-2 siRNA. *Sci. Rep.* **2015**, *4*, 6878.
(27) Yan, L.; Crayton, S. H.; Thawani, J. P.; Amirshaghaghi, A.; Tsourkas, A.; Cheng, Z. A pH-Responsive Drug-Delivery Platform Based on Glycol Chitosan-Coated Liposomes. *Small* **2015**, *11*, 4870−4874.
(28) Yang, G.; Xu, L.; Xu, J.; Zhang, R.; Song, G.; Chao, Y.; Feng, L.; Han, F.; Dong, Z.; Li, B.; Liu, Z. Smart Nanoreactors for pH-Responsive Tumor Homing, Mitochondria-Targeting, and Enhanced Photodynamic-Immunotherapy of Cancer. *Nano Lett.* **2018**, *18*, 2475−2484.
(29) Chen, H.; Tian, J.; He, W.; Guo, Z. H_2O_2-Activatable and O_2-Evolving Nanoparticles for Highly Efficient and Selective Photodynamic Therapy against Hypoxic Tumor Cells. *J. Am. Chem. Soc.* **2015**, *137*, 1539−1547.
(30) Ma, P.; Xiao, H.; Yu, C.; Liu, J.; Cheng, Z.; Song, H.; Zhang, X.; Li, C.; Wang, J.; Gu, Z.; Lin, J. Enhanced Cisplatin Chemotherapy by Iron Oxide Nanocarrier-Mediated Generation of Highly Toxic Reactive Oxygen Species. *Nano Lett.* **2017**, *17*, 928−937.
(31) Chen, Q.; Feng, L.; Liu, J.; Zhu, W.; Dong, Z.; Wu, Y.; Liu, Z. Intelligent Albumin-MnO_2 Nanoparticles as pH-/H_2O_2-Responsive Dissociable Nanocarriers to Modulate Tumor Hypoxia for Effective Combination Therapy. *Adv. Mater.* **2016**, *28*, 7129−7136.
(32) Prasad, P.; Gordijo, C. R.; Abbasi, A. Z.; Maeda, A.; Ip, A.; Rauth, A. M.; DaCosta, R. S.; Wu, X. Multifunctional Albumin-MnO_2 Nanoparticles Modulate Solid Tumor Microenvironment by Attenuating Hypoxia, Acidosis, Vascular Endothelial Growth Factor and Enhance Radiation Response. *ACS Nano* **2014**, *8*, 3202−3212.
(33) Cheng, Y.; Cheng, H.; Jiang, C.; Qiu, X.; Wang, K.; Huan, W.; Yuan, A.; Wu, J.; Hu, Y. Perfluorocarbon Nanoparticles Enhance Reactive Oxygen Levels and Tumour Growth Inhibition in Photodynamic Therapy. *Nat. Commun.* **2015**, *6*, 8785.
(34) Gao, M.; Liang, C.; Song, X.; Chen, Q.; Jin, Q.; Wang, C.; Liu, Z. Erythrocyte-Membrane-Enveloped Perfluorocarbon as Nanoscale Artificial Red Blood Cells to Relieve Tumor Hypoxia and Enhance Cancer Radiotherapy. *Adv. Mater.* **2017**, *29*, 1701429.
(35) Jia, Y.; Duan, L.; Li, J. Hemoglobin-Based Nanoarchitectonic Assemblies as Oxygen Carriers. *Adv. Mater.* **2016**, *28*, 1312−1318.
(36) Shen, Z.; Chen, T.; Ma, X.; Ren, W.; Zhou, Z.; Zhu, G.; Zhang, A.; Liu, Y.; Song, J.; Li, Z.; Ruan, H.; Fan, W.; Lin, L.; Munasinghe, J.; Chen, X.; Wu, A. Multifunctional Theranostic Nanoparticles Based on Exceedingly Small Magnetic Iron Oxide Nanoparticles for T1-Weighted Magnetic Resonance Imaging and Chemotherapy. *ACS Nano* **2017**, *11*, 10992−11004.
(37) Nowis, D.; Makowski, M.; Stoklosa, T.; Legat, M.; Issat, T.; Golab, J. Direct Tumor Damage Mechanisms of Photodynamic Therapy. *Acta Biochim. Polym.* **2005**, *52*, 339−352.
(38) Jiang, F.; Robin, A. M.; Katakowski, M.; Tong, L.; Espiritu, M.; Singh, G.; Chopp, M. Photodynamic Therapy with Photofrin in Combination with Buthionine Sulfoximine (BSO) of Human Glioma in the Nude Rat. *Lasers Med. Sci.* **2003**, *18*, 128−133.
(39) Liang, H.; Zhou, Z.; Luo, R.; Sang, M.; Liu, B.; Sun, M.; Qu, W.; Feng, F.; Liu, W. Tumor-Specific Activated Photodynamic Therapy with an Oxidation-Regulated Strategy for Enhancing Anti-Tumor Efficacy. *Theranostics* **2018**, *8*, 5059−5071.
(40) Zhang, W.; Lu, J.; Gao, X.; Li, P.; Zhang, W.; Ma, Y.; Wang, H.; Tang, B. Enhanced Photodynamic Therapy by Reduced Levels of

https://dx.doi.org/10.1021/acsnano.0c03080
ACS Nano 2020, 14, 11225−11237

Intracellular Glutathione Obtained By Employing a Nano-MOF with Cu^{II} as the Active Center. *Angew. Chem., Int. Ed.* **2018**, *57*, 4891−4896.
(41) Yang, B.; Chen, Y.; Shi, J. Reactive Oxygen Species (ROS)-Based Nanomedicine. *Chem. Rev.* **2019**, *119*, 4881−4985.
(42) He, D.; Hai, L.; He, X.; Yang, X.; Li, H. Glutathione-Activatable and O_2/Mn^{2+}-Evolving Nanocomposite for Highly Efficient and Selective Photodynamic and Gene-Silencing Dual Therapy. *Adv. Funct. Mater.* **2017**, *27*, 1704089.
(43) Xu, J.; Han, W.; Yang, P.; Jia, T.; Dong, S.; Bi, H.; Gulzar, A.; Yang, D.; Gai, S.; He, F.; Lin, J.; Li, C. Tumor Microenvironment-Responsive Mesoporous MnO_2-Coated Upconversion Nanoplatform for Self-Enhanced Tumor Theranostics. *Adv. Funct. Mater.* **2018**, *28*, 1803804.
(44) Wang, S.; Li, F.; Qiao, R.; Hu, X.; Liao, H.; Chen, L.; Wu, J.; Wu, H.; Zhao, M.; Liu, J.; Chen, R.; Ma, X.; Kim, D.; Sun, J.; Davis, T. P.; Chen, C.; Tian, J.; Hyeon, T.; Ling, D. Arginine-Rich Manganese Silicate Nanobubbles as a Ferroptosis-Inducing Agent for Tumor-Targeted Theranostics. *ACS Nano* **2018**, *12*, 12380−12392.
(45) Cheng, Y.; Yang, F.; Zhang, K.; Zhang, Y.; Cao, Y.; Liu, C.; Lu, H.; Dong, H.; Zhang, X. Non-Fenton-Type Hydroxyl Radical Generation and Photothermal Effect by Mitochondria-Targeted WSSe/MnO_2 Nanocomposite Loaded with Isoniazid for Synergistic Anticancer Treatment. *Adv. Funct. Mater.* **2019**, *29*, 1903850.
(46) Lin, L.; Song, J.; Song, L.; Ke, K.; Liu, Y.; Zhou, Z.; Shen, Z.; Li, J.; Yang, Z.; Tang, W.; Niu, G.; Yang, H.; Chen, X. Simultaneous Fenton-Like Ion Delivery and Glutathione Depletion by MnO_2-Based Nanoagent to Enhance Chemodynamic Therapy. *Angew. Chem., Int. Ed.* **2018**, *57*, 4902−4906.
(47) Xu, F.; Zhu, J.; Lin, L.; Zhang, C.; Sun, W.; Fan, Y.; Yin, F.; van Hest, J. C. M.; Wang, H.; Du, L.; Shi, X. Multifunctional PVCL Nanogels with Redox-Responsiveness Enable Enhanced MR Imaging and Ultrasound-Promoted Tumor Chemotherapy. *Theranostics* **2020**, *10*, 4349−4358.
(48) Zhang, M.; Xing, L.; Ke, H.; He, Y.; Cui, P.; Zhu, Y.; Jiang, G.; Qiao, J.; Lu, N.; Chen, H.; Jiang, H. MnO_2-Based Nanoplatform Serves as Drug Vehicle and MRI Contrast Agent for Cancer Theranostics. *ACS Appl. Mater. Interfaces* **2017**, *9*, 11337−11344.
(49) Lee, S. J.; Koo, H.; Jeong, H.; Huh, M. S.; Choi, Y.; Jeong, S. Y.; Byun, Y.; Choi, K.; Kim, K.; Kwon, I. C. Comparative Study of Photosensitizer Loaded and Conjugated Glycol Chitosan Nanoparticles for Cancer Therapy. *J. Controlled Release* **2011**, *152*, 21−29.
(50) Chen, Y.; Ye, D.; Wu, M.; Chen, H.; Zhang, L.; Shi, J.; Wang, L. Break-Up of Two-Dimensional MnO_2 Nanosheets Promotes Ultrasensitive pH-Triggered Theranostics of Cancer. *Adv. Mater.* **2014**, *26*, 7019−7026.
(51) Hou, W.; Xia, F.; Alves, C. S.; Qian, X.; Yang, Y.; Cui, D. MMP2-Targeting and Redox-Responsive PEGylated Chlorin e6 Nanoparticles for Cancer Near-Infrared Imaging and Photodynamic Therapy. *ACS Appl. Mater. Interfaces* **2016**, *8*, 1447−1457.
(52) Zhu, J.; Li, Z.; Zhang, C.; Lin, L.; Cao, S.; Che, H.; Shi, X.; Wang, H.; van Hest, J. C. M. Single Enzyme Loaded Nanoparticles for Combinational Ultrasound-Guided Focused Ultrasound Ablation and Hypoxia-Relieved Chemotherapy. *Theranostics* **2019**, *9*, 8048−8060.
(53) Riccardi, C. M.; Cole, K. S.; Benson, K. R.; Ward, J. R.; Bassett, K. M.; Zhang, Y.; Zore, O. V.; Stromer, B.; Kasi, R. M.; Kumar, C. V. Toward "Stable-On-The-Table" Enzymes: Improving Key Properties of Catalase by Covalent Conjugation with Poly(acrylic Acid). *Bioconjugate Chem.* **2014**, *25*, 1501−1510.
(54) Phua, S. Z. F.; Yang, G.; Lim, W. Q.; Verma, A.; Chen, H.; Thanabalu, T.; Zhao, Y. Catalase-Integrated Hyaluronic Acid as Nanocarriers for Enhanced Photodynamic Therapy in Solid Tumor. *ACS Nano* **2019**, *13*, 4742−4751.
(55) Sun, W.; Thies, S.; Zhang, J.; Peng, C.; Tang, G.; Shen, M.; Pich, A.; Shi, X. Gadolinium-Loaded Poly(N-vinylcaprolactam) Nanogels: Synthesis, Characterization, and Application for Enhanced Tumor MR Imaging. *ACS Appl. Mater. Interfaces* **2017**, *9*, 3411−3418.
(56) Yang, G.; Xu, L.; Chao, Y.; Xu, J.; Sun, X.; Wu, Y.; Peng, R.; Liu, Z. Hollow MnO_2 as a Tumor-Microenvironment-Responsive Biodegradable Nano-Platform for Combination Therapy Favoring Antitumor Immune Responses. *Nat. Commun.* **2017**, *8*, 902.
(57) Chen, W.; Luo, G.; Zhang, X. Recent Advances in Subcellular Targeted Cancer Therapy Based on Functional Materials. *Adv. Mater.* **2019**, *31*, 1802725.
(58) Su, L.; Li, R.; Khan, S.; Clanton, R.; Zhang, F.; Lin, Y.-N.; Song, Y.; Wang, H.; Fan, J.; Hernandez, S.; Butters, A. S.; Akabani, G.; MacLoughlin, R.; Smolen, J.; Wooley, K. L. Chemical Design of Both a Glutathione-Sensitive Dimeric Drug Guest and a Glucose-Derived Nanocarrier Host to Achieve Enhanced Osteosarcoma Lung Metastatic Anticancer Selectivity. *J. Am. Chem. Soc.* **2018**, *140*, 1438−1446.
(59) Sun, Q.; Ojha, T.; Kiessling, F.; Lammers, T.; Shi, Y. Enhancing Tumor Penetration of Nanomedicines. *Biomacromolecules* **2017**, *18*, 1449−1459.
(60) Friedrich, J.; Seidel, C.; Ebner, R.; Kunz-Schughart, L. A. Spheroid-Based Drug Screen: Considerations and Practical Approach. *Nat. Protoc.* **2009**, *4*, 309−324.

https://dx.doi.org/10.1021/acsnano.0c03080
ACS Nano 2020, 14, 11225−11237